RESEARCH ARTICLE | APRIL 23 2025

Magnetic Mie resonances in negative-index medium

Viktoriia E. Babicheva

APL Photonics 10, 046117 (2025)
https://doi.org/10.1063/5.0257357
CHORUS

Magnetic Mie resonances in negative-index medium

Cite as: APL Photon. **10**, 046117 (2025); doi: 10.1063/5.0257357
Submitted: 9 January 2025 • Accepted: 10 April 2025 •
Published Online: 23 April 2025

Viktoriia E. Babicheva[a]

AFFILIATIONS

Department of Electrical and Computer Engineering, University of New Mexico, Albuquerque, New Mexico 87131, USA

[a]Author to whom correspondence should be addressed: vbb@unm.edu

ABSTRACT

High-refractive-index nanoantennas have attracted significant attention lately because of the strong excitations of electric and magnetic resonances in these nanoantennas. Here, we theoretically investigate the excitation of multipolar Mie resonances in high-refractive-index nanoantennas that are immersed in a negative-index medium. Our analysis shows a significant enhancement of magnetic resonances in this case. Furthermore, the magnetic dipolar and quadrupolar resonances exhibit a π-shift compared to these magnetic resonances in a conventional medium, which stems from the "left-handedness" of the negative-index medium. As a result, the spectral regions where electric and magnetic resonances are in-phase or out-of-phase complement, or opposite, to those in a conventional medium. Most importantly, we demonstrate nanoantenna magnetic resonances in two practical cases of negative-index media realized with common materials, such as multilayer structures with surface waves with negative effective mode index and fishnet metamaterial. These findings represent significant progress toward the realization of hybrid emitting structures that exhibit transitions with both electric and magnetic dipolar characteristics and pave the way for greater flexibility in controlling radiation patterns from quantum emitters.

I. INTRODUCTION

Nanoscale structures have emerged as promising candidates for optical applications, photonic devices, ultra-thin functional elements and metasurfaces,[1] sensing,[2,3] enhanced light–matter interaction,[4–7] and microscopy with subwavelength resolution.[8] This is enabled by their ability to enhance optical resonances and manipulate light absorption and scattering. Nanoantennas made of various materials and shapes have been utilized as building blocks to design ultra-thin nanostructures, commonly referred to as metasurfaces. Recently, high-refractive-index dielectrics—silicon, germanium, and III–V compounds—have emerged as viable platforms for subwavelength nanoantennas, and high-refractive-index metasurfaces are leading to revolutionizing the field of metaphotonics.[9,10] The latter, an emerging multidisciplinary field, establishes designing principles for manipulating electromagnetic energy in complex photonic structures through engineered electric and magnetic excitations. This allows for precise control of linear and nonlinear optical properties with practical domains spanning optical switching, negative- and near-zero refractive-index medium, chiral bioimaging, and others.[11]

Advancements in nanofabrication techniques and the exploration of magnetic quantum emitters, such as rare-earth ions, have sparked renewed interest in the magnetic properties of spontaneous emission. This has led to the development of specialized nanophotonic structures that enable enhanced spontaneous emission of the magnetic dipole,[12] and this offers exciting opportunities to design optical nanocavities with unprecedented control over the magnetic density of the photon states and the enhanced brightness of the magnetic emitters. Compared to plasmonic nanoantennas, high-refractive-index dielectrics have the advantage of supporting excitations of both electric and magnetic resonances in simple-shaped nanoantennas, such as spheres or disks.[1] When the electric (ED) and magnetic dipolar (MD) polarizabilities of the nanoantenna are equal in magnitude and phase, the so-called first Kerker condition is satisfied,[13] leading to near-zero backward scattering (Kerker effect). The resonant interplay and overlap of different multipoles in these high-refractive-index nanoantennas offer unprecedented

control over light scattering, leading to the design of more efficient subwavelength antennas.[14,15]

Negative reflection and negative refraction are intriguing optical phenomena that have been extensively explored through various approaches, including double-negative metamaterials and hyperbolic metamaterials. The left-handed medium exhibits fascinating electromagnetic properties, such as negative refraction and backward wave propagation, and can be realized using the so-called negative-index medium. The latter can be designed from plasmonic or dielectric nanostructures to mimic the refractive index that has an effective negative value in a particular spectral range. Designing a negative refractive index medium presents a significant challenge in achieving low loss because the material must be engineered to minimize attenuation while maintaining the desired optical properties. Ensuring minimal loss involves careful optimization of both material composition and structural design to balance effective refractive index characteristics with practical performance constraints.

The negative-index properties of the engineered medium can be observed when both effective permittivity ε and permeability μ are negative.[16,17] It is important to note that the correct sign must be chosen in the definition of the effective refractive index, which is $n_{NIM} = -\sqrt{(\varepsilon\mu)}$ if $\mu<0$ and $\varepsilon<0$, as required by causality.[18] Recent advances in anomalous refractive and reflective metasurfaces have achieved precise control over the light direction and polarization by exploiting engineered material responses and spatially varying phase shifts at the subwavelength scale.[19] Various metamaterials with an effective negative index have been proposed, including metal–dielectric multilayer structures with small or larger numbers of layers,[20–25] patterned fishnets,[26] cruciforms,[27] or other shapes,[28] as well as metal inclusions of different variations.[29,30] The development of all-angle reflectionless negative refraction in ideal photonic Weyl metamaterials demonstrates significant progress in achieving optimal control over light propagation and manipulation in complex optical systems.[31]

An experimental achievement of a two-dimensional negative-index medium within the blue and green domains of the visible range with direct geometric visualization of negative refraction has been reported.[20] A negative-index metamaterial in the ultraviolet range, composed of stacked plasmonic waveguides supporting antisymmetric modes, has been experimentally shown to achieve negative refraction for TM-polarized light at 365 nm, enabling subwavelength photolithography with a feature size of 160 nm.[8] A single-layer wide-angle negative-index metamaterial has been achieved using coupled plasmonic coaxial waveguides,[32] demonstrating an effective refractive index of –2 in the blue spectral region with a figure-of-merit exceeding eight and insensitivity to polarization at visible frequencies. In most cases, such metamaterials are designed to be used effectively as a continuous layer to control the propagation of light through them. Tunable directional scattering has been achieved from high-refractive-index particles dispersed within an anisotropic medium[33] or fabricated on top of it.[21] Optically induced negative refraction has been observed in a time-varying system, in which plasmonic antennas are strongly coupled to an epsilon-near-zero film.[34] Furthermore, biaxial van der Waals materials, which support in-plane hyperbolic phonon polaritons, have been demonstrated to be promising platforms for planar reflective and refractive optics.[35–39]

Here, we demonstrate multipolar Mie resonances in high-refractive-index nanoantennas within a negative-index medium, and we present a design utilizing a multilayer structure as a negative-index medium to enhance the optical response of nanoantennas inside or adjacent to them. We demonstrate that placing nanoantennas in this medium enhances the magnetic resonances of nanoantennas and causes them to be π-shifted in phase compared to the case of nanoantennas in a conventional medium. We expand the Kerker condition for the nanoantennas in a negative-index medium, identifying a spectral region with enhanced forward scattering between electric and magnetic dipolar resonances. Most importantly, from the practical point of view, we confirm the excitation of these resonances in two realistic cases of negative-index media using common materials in a multilayer configuration. In both cases, we see that the Mie resonances are excited in accordance with the effective negative-index waves supported by these multilayer structures. We demonstrate that a silicon nanosphere with a radius of 15–60 nm can experience significant enhancement of its magnetic resonances when confined in the air channel of a multilayer fishnet metamaterial, and similar properties can be observed using other negative-index metamaterials. This progress enables greater control over radiation patterns from quantum emitters with dual electric and magnetic dipolar characteristics.

II. SILICON NANOANTENNA ARRAYS IN NIM

To start with, we consider high-refractive-index nanoantennas immersed in an ideal negative-index medium (NIM) and investigate the properties of these nanoantennas in a periodic lattice. In a conventional—positive-index—medium, *E*-field, *H*-field, and the propagation vector *k* follow the right-hand rule. In turn, *E*, *H*, and *k* follow the left-hand rule in a left-handed medium. In essence, it means that the *H*-field experiences a π phase shift relative to the conventional case.[16] Alternatively, one can view the *k*-vector as having an opposite direction to that of energy propagation. Structured light refers to light that has a non-uniform phase distribution across its transverse profile, such as optical vortices, Bessel beams, and other complex wavefronts.[40,41] When this structured light interacts with nanoantennas, their arrays, and metasurfaces, it can induce novel optical responses as a result of spatially varying electric and magnetic fields. The properties of structured light illuminating nanoantennas are of great interest in photonics and nanophotonics as this can lead to enhanced scattering, absorption, and polarization effects.

The applicability of Mie theory and the coupled-multipole model to the interaction of electromagnetic waves with scatterers embedded in NIM follows from the fundamental principles governing wave propagation and scattering. However, their direct application requires careful modification to accommodate the unique electromagnetic properties of NIMs, particularly the inversion of phase velocity relative to energy flow (the Poynting vector and wavevector are antiparallel) and nontrivial boundary conditions. Although Mie theory and the coupled multipole model remain formally applicable to scattering problems in NIMs, their direct use requires a rigorous reformulation of the field expansions, scattering coefficients, and interaction tensors to correctly describe the unique wave dynamics inherent to negative-index environments.

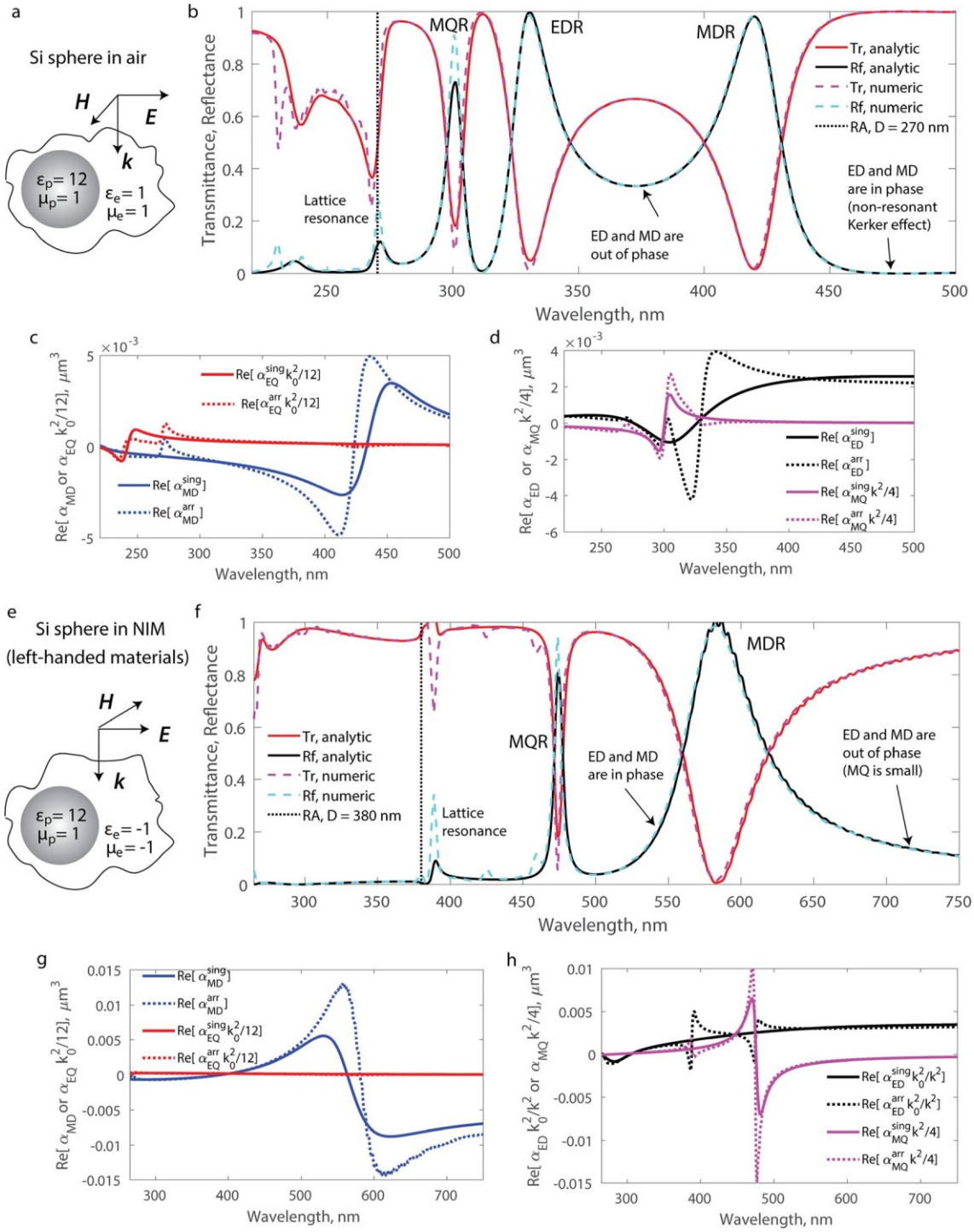

FIG. 1. (a) Schematic of a silicon nanosphere ($\varepsilon_p = 12$ and $\mu_p = 1$) in air ($\varepsilon_e = 1$ and $\mu_e = 1$). (b) Transmittance and reflectance of a square nanosphere array with $D = 270$ nm. (c) and (d) Real part of the effective polarizabilities of the single nanoantenna (marked "sing") and nanoantenna in the array (marked "arr") for ED, MD, EQ, and MQ. (e) Schematic of the silicon nanosphere ($\varepsilon_p = 12$ and $\mu_p = 1$) in NIM $\varepsilon_e = -1$ and $\mu_e = -1$. (f) Transmittance and reflectance of a square nanosphere array in NIM with $D = 380$ nm. (g) and (h) Real part of the effective polarizabilities of the single nanoantenna (marked "sing") and the nanoantenna in the array (marked "arr") for ED, MD, EQ, and MQ. The phase of the MD resonance is π-shifted relative to the MD resonance in the medium with a positive index [compare panels (c) and (g)]. The vertical dotted black lines (denoted RA) in panels (b) and (f) correspond to the wavelength of the Rayleigh anomaly.

The wavevector k and the Poynting vector S have opposite directions, requiring adapted definitions of forward and backward scattering, as conventional conservation laws of angular momentum can lead to counterintuitive results. The coupled-multipole model, a more generalized approach to treating multiple scatterers in the lattice, relies on the induced multipolar moments. Modification of spherical harmonics, Bessel functions, and recalculation of scattering coefficients in the complex plane need to be implemented to accurately extend the Mie theory and the coupled multipole model to NIMs.

Mie theory, formulated as an exact solution to Maxwell's equations for spherical scatterers in homogeneous isotropic media, inherently relies on the expansion of incident and scattered fields into vector spherical harmonics. The key components governing its validity in NIMs include field representations in spherical coordinates, modified spherical harmonic expansions, and analytical continuation in complex k-space. Since Maxwell's equations remain form-invariant under coordinate transformations, Mie theory remains formally applicable. However, the constitutive relations $D \neq \varepsilon E$ and $B \neq \mu H$ require modifications, as permittivity ε and permeability μ can both be negative, leading to reversed boundary conditions at the scatterer–medium interface. The vector spherical wave functions used to describe the fields must be adapted to account for the reversal of phase velocity and energy flow in NIMs. The spherical Hankel functions, which describe outgoing waves in conventional media, must be adapted to support energy flow reversal. This involves using the appropriate branch of Hankel functions to represent waves propagating in NIMs. Ensuring correct branch selection in complex-k space is critical to obtaining physically meaningful solutions and avoiding singularity when Mie coefficients are derived from boundary conditions, thereby ensuring field continuity when extended to NIMs. Mie coefficients, derived from matching conditions, require analytical continuation into complex frequency space to ensure causality and stability in the presence of NIM-specific dispersion.

Our analysis begins with a conventional silicon nanoantenna with $\varepsilon_p = 12$ (with negligible dispersion and losses) and $\mu_p = 1$, with a radius of $R = 60$ nm in air. The surrounding material has a permittivity and permeability of $\varepsilon_e = \mu_e = 1$ [Fig. 1(a)]. We calculate the ED, MD, electric quadrupolar (EQ), and magnetic quadrupolar (MQ) polarizabilities of a single nanoantenna. We also calculate the effective polarizability values in the array (with a period $D = 270$ nm) as well as the reflectance and transmittance of the array [Figs. 1(b)–1(d)]. Throughout this work, we show the real part of the effective nanoantenna polarizabilities to illustrate changes in their sign at multipolar resonances. The sign change of the real part of the nanoantenna polarizability is accompanied by a maximum of the imaginary part, which is not shown in the figures. In Fig. 1(b), for wavelengths longer than the Rayleigh anomaly (RA, vertical dotted black line), one can observe that the ED, MD, and MQ polarizabilities exhibit resonances that result in an increase in reflectance and a decrease in transmittance through the array. In this conventional case, the multipolar polarizabilities are comparable in magnitude but out of phase between the ED and MD resonances. In this spectral range, the reflectance is higher than the reflectance in the wavelength range where resonances are in phase (spectral red side of the MD resonance). Correspondingly, the transmittance between the ED and MD resonances is lower than transmittance when the ED and MD resonances are in phase. The non-resonant Kerker effect is observed when the ED and MD resonances are in phase and have equal magnitude. The analytical calculations of reflectance and transmittance agree well with full-wave numerical simulations, which do not include any approximations [see Fig. 1(b)].

In the second case, the situation changes drastically when we consider the same silicon nanoantenna ($\varepsilon_p = 12$, $\mu_p = 1$, $R = 60$ nm) in NIM with $\varepsilon_e = 1$ and $\mu_e = 1$ [dispersion and losses are neglected, Fig. 1(e)]. Here, for full-wave numerical simulations, we use hypothetical materials with negative permittivity and permeability. The ED resonance is relatively weak, but the ED polarizability remains almost constant for $\lambda > 400$ nm and is comparable in magnitude with the MD polarizability. The MD and MQ resonances appear at a longer wavelength compared to the case of the same nanoantennas in free space (air), and therefore, for the array analysis, we select a larger array period $D = 380$ nm. In Fig. 1(f), for wavelengths longer than the Rayleigh anomaly, an increase in reflectance and a decrease in transmittance correspond to MD and MQ resonances. The MD resonance is strong, and its phase is π-shifted relative to the MD resonance in the medium with a positive index [compare panels (c) and (g) in Fig. 1]. This occurs because of the π shift of the H-field oscillations in the left-handed medium. Thus, the ED and

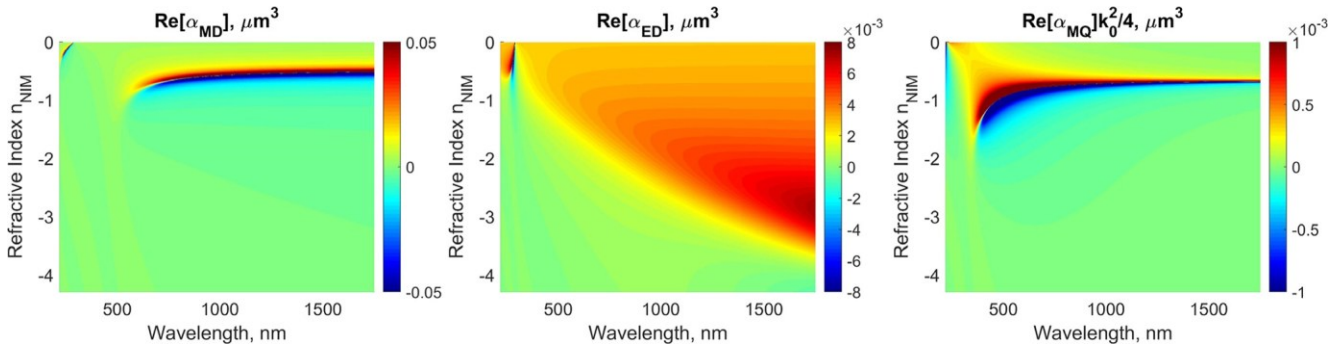

FIG. 2. Real part of nanoantenna polarizability for single silicon nanosphere with $R = 60$ nm (with $\varepsilon_p = 12$ and $\mu_p = 1$) in NIM with refractive index $n_{NIM} = -\sqrt{(\varepsilon_e \mu_e)}$, where ε_e is varied and $\mu_e = \varepsilon_e$: (a) MD, (b) ED, and (c) MQ polarizabilities.

MD resonances are excited in phase on the spectral blue side of the MD resonance, and the reflectance of the array is decreased compared to the values on the spectral red side of the MD resonance, where the ED and MD resonances are excited out of phase. The MQ resonance is narrower and more pronounced than the ED resonance, and it is responsible for a peak in reflectance and a dip in transmittance. However, outside the spectral region with resonant excitations, the MQ polarizability is much smaller in value than the ED polarizability. Similarly to the conventional case, the analytical calculations of reflectance and transmittance of the nanoantenna array agree well with numerical simulations [see Fig. 1(f)].

As the host medium surrounding the nanoantenna can vary, let us consider multipolar resonances of a silicon nanosphere in NIM with different refractive indices. Figure 2 shows the changes in the polarizability of the nanoantenna in the medium $n_{NIM} = -\sqrt{(\varepsilon_e \mu_e)}$, where $\mu_e = \varepsilon_e$ and the n_{NIM} value is varied. For $\lambda > 500$ nm, we observe a strong MD resonance at $n_{NIM} = -0.54$ [Fig. 2(a)] and an MQ resonance at $n_{NIM} = -0.66$ [Fig. 2(c)]. The ED resonance is at $\lambda = 285$ nm and $n_{NIM} = -0.25$ [Fig. 2(b)]. Figure 2 presents calculations only for the case $\mu_e = \varepsilon_e$, but additional calculations show that for various ratios of μ_e/ε_e, the resonant n_{NIM} varies. However, the excitation conditions of the MD and MQ resonances remain close and $n_{NIM,MD} \approx n_{NIM,MQ} \approx 0.1$–$0.2$. These MD and MQ resonances for a surrounding medium with $|n_{NIM}| < 1$ are much stronger than for the case of $\varepsilon_e = \mu_e = -1$ considered above [e.g., compare the value of MD polarizability for $n_{NIM} = -1$ and $n_{NIM} = -0.54$ in Fig. 2(a)].

III. SILICON NANOANTENNAS AND SURFACE WAVES

Now, let us consider a structure with realistic materials where no hypothetical materials are involved. Reference 22 provides a guideline for designing a simple multilayer structure that supports surface waves, in particular surface plasmon polaritons (SPPs), with negative group velocity. We choose one of the designs described in Ref. 22 and work with a silver surface as an infinite substrate and a 10 nm thick high-refractive-index material on top of the silver [Fig. 3(a)]. Although the initial design in Ref. 22 suggests using gallium phosphide as a thin dielectric layer, we find it more practical to consider amorphous silicon, as it can be deposited using conventional thin-film deposition techniques, such as electron-beam evaporation or sputtering, rather than the need to grow III–V compounds or other crystalline materials. Other practical designs can include low- and moderate-refractive-index materials, such as silicon oxide or nitride, because they can also be deposited on a silver surface. However, as demonstrated in Ref. 22, reducing the refractive index of the thin dielectric layer leads to a shift in the spectral range, and the highest figure-of-merit moves toward shorter wavelengths.

The absorption is determined by computing the difference between incident, reflected, and transmitted waves. Full-wave numerical simulations incorporate Floquet–Bloch boundary conditions in the transverse directions to model the infinite periodicity of the nanoantenna array under oblique incidence. Perfectly matched layers are applied to the computational domain along the propagation axis to prevent artificial reflections. Silver is modeled as an infinitely thick substrate to prevent transmission, and its material response is fully accounted for by incorporating dispersion using a frequency-dependent permittivity, ensuring accurate representation of plasmonic effects and the excitation of surface plasmon polaritons at the metal–dielectric interface. Absorption calculations are performed by analyzing the incidence of a plane wave on a periodic array of silicon nanoantennas on top of a silver surface with a 10 nm thin dielectric spacer. The array is lifted 200 nm above the dielectric to prevent the formation of hot spots in the narrow gaps between the sphere and the substrate. The wave is incident on the array at 5°, which has an insignificant effect on the nanoantenna response but introduces a symmetry break, as well as excitation of surface waves. The local field enhancement due to surface plasmon polaritons at the metal–dielectric interface contributed to the observed absorption characteristics, mimicking the effect of a negative-index environment.

In Fig. 3(b), we present a comparison of resonances supported by the nanoantenna array when situated atop the metal surface (marked "SPP" in the legend) and when surrounded by the modeled negative-index medium (marked "NIM"). The near-field of the silicon nanoantenna couples to SPPs at the metal–dielectric interface, leading to enhanced absorption due to the excitation of bound electromagnetic modes with negative group velocity. This coupling modifies the local density of the optical states, effectively increasing energy dissipation in the nanoantenna because of the resonance

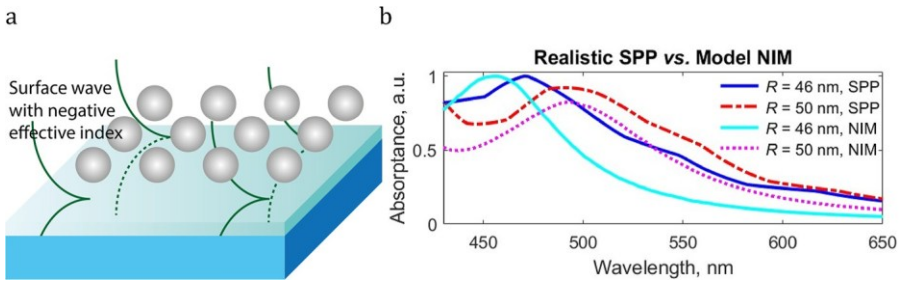

FIG. 3. Realization of NIM with surface waves. (a) Schematic of the structure: silicon nanoantenna array on top of a metal surface (blue) with a thin dielectric layer (green) that facilitates negative velocity. We consider silver as an infinite metal substrate and 10 nm silicon as a thin dielectric layer. (b) Absorption in silicon nanoantennas for the case with surface waves (marked "SPP") and the model with negative-index medium (marked "NIM") with $\varepsilon_e = -1$ and $\mu_e = -1$. Silicon nanoantennas are spheres with radius $R = 46$ or 50 nm, and the spacing between the nanoantennas in each in-plane direction is 200 nm.

resembling one in NIM. These nanoantenna resonances are identified by an increase in absorptance. It is apparent that these nanoantenna resonances uniformly undergo a wavelength shift toward longer wavelengths, with an increase in the sphere radius. Surface waves with a negative index effectively mimic the conditions of a model with a negative index. Nanoantenna resonances in both scenarios exhibit striking similarities, and their response to changes in nanoantenna size remains consistent.

IV. SILICON NANOANTENNAS IN FISHNET METAMATERIALS

Now, let us explore another instance of a practical structure, once again using realistic materials without reliance on hypothetical substances. To simulate the case of a nanosphere surrounded by a negative-index medium, we employ a multilayer fishnet structure, demonstrated in Ref. 26, as a metamaterial supporting negative-index modes (Fig. 4). The fishnet has a period $p = 860$ nm, wide stripe width $a = 564$ nm, narrow stripe width $b = 264$ nm, silver layer thickness $t_{Ag} = 30$ nm, and magnesium fluoride layer thickness $t_{MgF2} = 50$ nm. The total number of layers in our fishnet structure is 44 (22 pairs).

For fishnet analysis, we perform both analytical calculations and full-wave numerical simulations. The former is based on coupled dipole–quadrupole equations following the approach in Refs. 42–44 with the polarizability of the silicon nanoantenna calculated with the Mie theory.[10,45,46] Generalized expressions for the case of a nanoantenna and surrounding media with electric and magnetic responses are derived in the Appendix. For full-wave numerical simulations, we calculate a realistic multilayer fishnet metamaterial with a silicon nanoantenna inside it [Fig. 4(a)]. We model the fishnet unit cell with periodic boundary conditions in the transverse directions and perfectly matched layers in the direction of wave propagation.

First, we analyze the modes supported by the fishnet without the nanoantenna. For that, we detect the field along the air channel and perform a spatial Fourier transformation (FT) to obtain the spatial harmonics of the propagating wave. Multiple points along the wave propagation direction are used in the spatial FT in the channel center in the transverse directions. In Fig. 4(b), we show the result of FT normalized to its maximum at each wavelength. This fishnet metamaterial exhibits strong dispersion, resulting in a wide range of negative indices. The strongest mode has $|n_{NIM}| < 1$ at $1500\text{ nm} < \lambda < 1650$ nm and, in particular, $n_{NIM} = -0.67$ at $\lambda = 1605$ nm. This mode has the lowest losses and mainly defines light propagation through the fishnet (reported in Ref. 26). However, there are also weaker modes supported by the channel: the 2nd mode has $n_{NIM} = -0.45$ at $\lambda = 1740$ nm, the 3rd mode has $n_{NIM} = -0.56$ at $\lambda = 1840$ nm, and the 4th mode has $n_{NIM} = -0.56$ at $\lambda = 1910$ nm [marked as stars in Fig. 4(b)]. We consider the case of a silicon nanosphere with $\varepsilon_p = 12$ and $\mu_p = 1$. Analytical calculations show that resonances occur at n_{NIM} values of $-0.7 \ldots -0.55$ [Figs. 2 and 4(c)]. For $\mu_e = \varepsilon_e$, the MD resonance is at $n_{NIM} = -0.54$ [Fig. 4(a)]; and for $\mu_e = 0.55\varepsilon_e$, the MD resonance is at $n_{NIM} = -0.70$

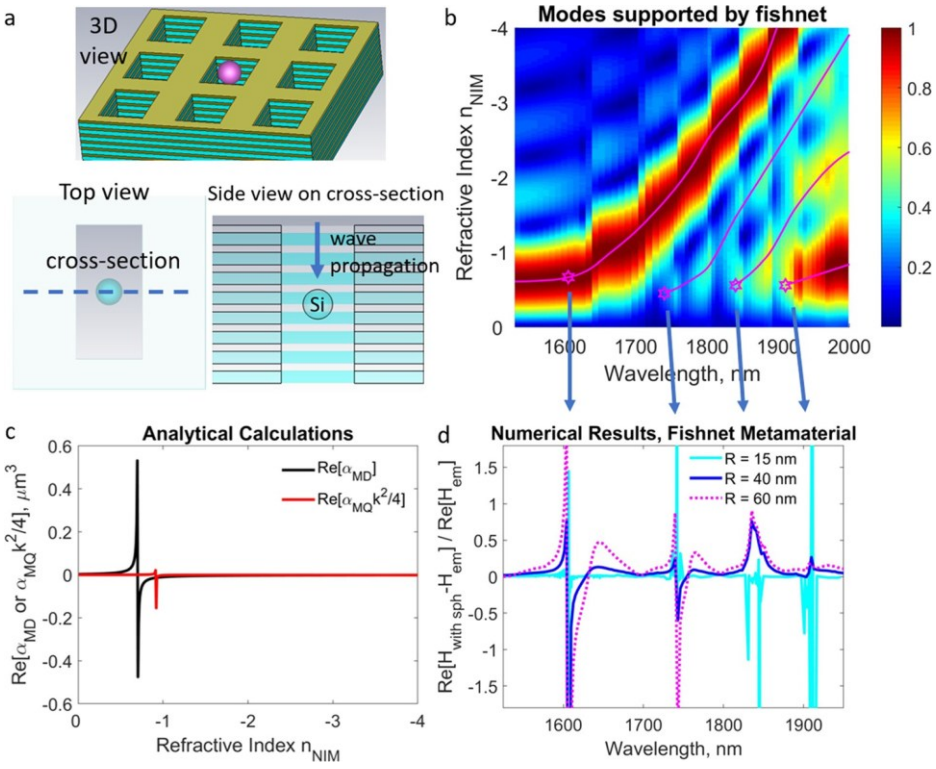

FIG. 4. (a) Schematic of the fishnet nanostructure built of silver and magnesium fluoride layers with a silicon nanosphere inside the channel. This panel shows three-dimensional (3D), top, and side views. (b) Fourier transformation (FT) of the field inside the fishnet air channel detected without the nanoantenna. The maxima in FT indicate multiple modes supported by the metamaterial (marked by the solid lines). The stars mark the wavelength at which nanoantenna resonances are observed. (c) The real part of the magnetic dipolar and quadrupolar polarizabilities of the nanoantenna calculated analytically for the single silicon nanosphere with $R = 60$ nm. The refractive index is defined as $n_{NIM} = -\sqrt{(\varepsilon_e \mu_e)}$, where $\mu_e = 0.55\,\varepsilon_e$ and ε_e is varied. (d) The relative increase in the H-field at the position of the sphere center ($H_{with\ sph}$) in comparison with the fishnet without a sphere (empty, H_{em}). The sphere radius is $R = 15$, 40, or 60 nm.

[Fig. 4(c), λ =1700 nm is used in calculations]. Resonance positions do not show visible changes for nanospheres of different sizes (radii R= 15–60 nm).

In the next step, we place the silicon nanosphere inside the fishnet channel and detect the relative spectral changes in the H-field with respect to the fishnet without the nanoantenna [Fig. 4(d)]. For the nanoantenna with radius R=40 nm, its scattering is relatively weak compared to the field propagating in the channel, so the fishnet modes are preserved, and we see H-field resonances very similar to Fig. 4(c). The four resonances in Fig. 1(d) correspond to the excitations of the four modes supported by the fishnet [shown in Fig. 4(b)]. Each mode has n_{NIM} in the range– 0.7 -0.55, and the nanoantenna responds resonantly by a local increase in the H-field. For the smaller nanoantenna with R=15 nm, resonances are observed at the same spectral positions, but the noise level is higher due to weaker scattering. In turn, light scattering from the nanoantenna with R =60 nm is relatively strong and disrupts the fishnet mode, resulting in distorted resonance profiles.

If more complex nanoparticles with anisotropic or multipolar responses are placed in the gaps, the resonances of the system will be modified due to additional degrees of freedom in the induced electric and magnetic polarizabilities. The overall behavior of the metalayer can then be actively controlled by tailoring the polarizabilities of these nanoparticles, allowing for tunable scattering, absorption, and coupling to surface waves. This scenario parallels the problem of a loop antenna radiating in the presence of a conducting sphere,[47] where the induced currents and fields on the sphere significantly alter the antenna's radiation pattern and impedance. It also relates to the problem of electromagnetic fields induced in inhomogeneous dielectric spheres by external sources,[48] where the internal field distribution and resulting scattering properties are governed by spatially varying permittivity and permeability, which influence the effective medium response of the system.

As the optical period of a metasurface increases, new diffraction orders emerge, leading to enhanced resonances that facilitate anomalous reflection. This phenomenon has been observed in all-dielectric gradient metasurfaces,[49] where spatially varying phase gradients enable efficient anomalous reflection of light at nontrivial angles without relying on conventional refractive index contrast. Similarly, in reconfigurable acoustic metagratings, the ability to engineer diffraction-mediated interactions allows for near-unity anomalous reflection efficiency by dynamically tuning structural parameters.[50] The interplay between multipolar resonances and diffraction effects in such metasurfaces provides a pathway for optimizing wavefront control across different spectral domains, expanding the potential for applications in optical and acoustic wave manipulation. The introduction of new diffraction orders in the nanoantenna array within NIM can lead to additional scattering channels, redistributing the energy among multiple directions and modifying the interference conditions that govern resonance enhancement. This can result in stronger coupling between multipolar Mie resonances and diffraction modes, potentially amplifying or suppressing specific resonances depending on the phase-matching conditions. Moreover, the interplay between diffraction and the unique left-handed properties of the NIM can potentially enable unconventional wavefront shaping, including negative-angle scattering or tailored radiation patterns distinct from conventional dielectric environments.

V. DISCUSSION

The confidence in the correctness of the presented results follows from a combination of rigorous theoretical analysis, numerical simulations, and agreement between different methods. Analytical calculations are validated against full-wave numerical simulations,

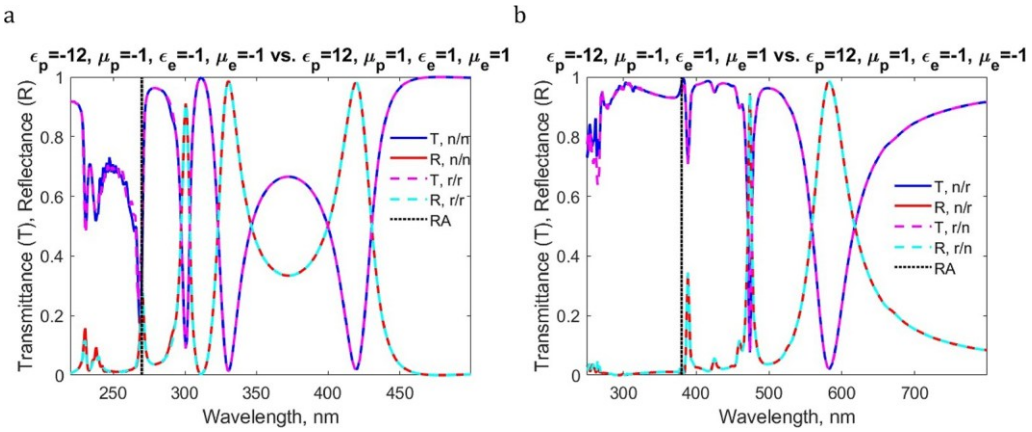

FIG. 5. Reflectance and transmittance obtained by analytical calculations of the arrays complementary to those shown in Fig. 1(a) Nanoparticles and the surrounding medium are NIM: $\varepsilon_p = -12$, $\mu_p = -1$, $\varepsilon_e = -1$, and $\mu_e = -1$ (marked "n/n" in the legend, "n" stands for "negative"). The corresponding complementary case is regular silicon nanoparticles in air [marked "r/r" in the legend, "r" stands for "regular"; the dashed cyan and red lines are the same as in Fig. 1(b)]. (b) NIM nanoparticles with $\varepsilon_p = -12$ and $\mu_p = -1$ is in air (marked "n/r" in the legend). The corresponding complementary case is regular silicon nanoparticles in NIM with $\varepsilon_e = -1$ and $\mu_e = -1$ [marked "r/n" in the legend; the dashed cyan and red lines are the same as in Fig. 1(f)]. The vertical dotted black lines (RA) on both panels correspond to the wavelength of the Rayleigh anomaly.

ensuring accuracy in predicting the behavior of nanoantennas in NIM [Figs. 1(b) and 1(f)]. Figure 5 demonstrates that swapping the signs of permittivity and permeability for both the nanoparticle and the surrounding medium does not alter the reflectance and transmittance spectra. This confirms the correctness of the results by illustrating the invariance of Maxwell's equations under simultaneous inversion of material parameters. The agreement between the complementary cases—regular silicon nanoparticles in air and negative-index nanoparticles in NIM—validates the theoretical predictions and supports the robustness of the analytical and numerical approaches.

In addition, the study tests the proposed concepts in two realistic configurations: a multilayer structure supporting surface waves with a negative effective mode index and a fishnet metamaterial exhibiting negative refractive index behavior. These test problems serve as practical demonstrations of the theoretical framework, confirming that the predicted multipolar resonances and their phase shifts persist under physically realizable conditions. The consistency between analytical models, numerical simulations, and experimental feasibility supports the reliability of the results.

The results reported in this work demonstrate the ability to engineer and control nanoantenna resonances through the interplay of multipolar excitations, particularly magnetic ones, in a structured negative-index environment, rather than rely solely on the nanoantenna's shape or material. It has been demonstrated in multiple previous studies that new phenomena emerge when the optical medium turns from uniform free space to an effective double-negative medium or plasmonic nanostructure. This work demonstrates how tailoring nanoantenna coupling to surface waves and channel modes can manipulate these effects and induce particularly strong magnetic resonances. This tunability can be further enhanced by artificially designed surrounding with more interesting properties, inducing highly tailored optical responses that are unattainable with conventional uniform surrounding or an engineered nanoantenna. Although the focus of this work remains on the intrinsic properties of the nanoantenna rather than the surrounding medium, we note that nonlinearity and coherent perfect absorption in epsilon-near-zero plasmonic waveguides can enable dynamic control over absorption and resonance conditions.[51] The case of coherent perfect absorption in epsilon-near-zero plasmonic waveguides is particularly interesting due to the possibility of developing a structured environment. Although it would be highly interesting to investigate how the nanoantenna behaves within such a plasmonic waveguide, including potential modifications to its multipolar resonances and coupling, this analysis is beyond the scope of the current study and will be addressed in future work. Gyrotropic heterostructures and the giant enhancement of nonreciprocity can be leveraged to induce unconventional multipolar resonances, as such structured material environments dramatically modify wave interactions,[52] reinforcing the broader principle that engineered resonances can be used to control wave propagation and scattering. Investigating the behavior of the nanoantenna within or in proximity to a gyrotropic heterostructure, where nonreciprocity can further modify its resonant response and scattering properties, would be an intriguing direction for future research, but it lies beyond the scope of the present work.

VI. CONCLUSIONS

In summary, we reported that the resonant magnetic response of a high-refractive-index nanoantenna can be enhanced by placing the nanoantenna in a surrounding with a negative refractive index. As the NIM has an H-field that is π-shifted relative to the conventional positive-index material, the magnetic resonances of the nanoantenna in this NIM also experience a π shift with respect to the conventional resonances. We took the next step in generalizing the Kerker condition for the case of the nanoantenna in a negative-index medium and demonstrated that the spectral region with increased forward scattering is between the electric and magnetic dipolar resonances. The reflectance increases on the spectral red side of the MD resonance because the ED and MD resonances are out of phase, and the reflectance decreases to a near-zero value (Kerker effect) between the MD and ED resonances where the resonances are in phase. If the signs of permittivity and permeability of the nanoantenna and the surrounding medium are reversed, the reflectance and transmittance spectra of the nanoantenna array do not change. To highlight the real-life manifestation of the observed phenomena, we showed that the magnetic resonances of the nanoantenna can be observed in a structure composed of realistic materials. The results with the surface waves revealed that when the wave exhibits an effective negative index, it creates an environment akin to a negative refractive index. We analyzed a nanoantenna in a multilayer fishnet, which is another example of a structure that provides artificial magnetism and effectively behaves as a medium with a negative refractive index. This metamaterial exhibits strong dispersion, which allows for the analysis of nanoantenna properties over a broad range of negative indices. We numerically demonstrated the excitation of magnetic resonances in the silicon sphere with radii of 15–60 nm in the fishnet structure and ascribed them to multiple modes supported by the fishnet metamaterial. These results demonstrate the potential of using a multilayer structure as a negative-index medium to enhance the optical response of nanoantennas, including their magnetic resonance, within or adjacent to them.

ACKNOWLEDGMENTS

This material is based on work supported, in part, by the National Science Foundation under Grant No. 2418519. This work was performed, in part, at the Center for Integrated Nanotechnologies, an Office of Science User Facility operated for the U.S. Department of Energy (DOE) Office of Science by Los Alamos National Laboratory (Contract No. 89233218CNA000001) and Sandia National Laboratories (Contract No. DE-NA-0003525).

AUTHOR DECLARATIONS

Conflict of Interest

The author has no conflicts to disclose.

Author Contributions

Viktoriia E. Babicheva: Investigation (lead); Writing – original draft (lead).

DATA AVAILABILITY

The data that support the findings of this study are available from the corresponding author upon reasonable request.

APPENDIX: ANALYTICAL EXPRESSIONS

1. Analytical expressions for single-particle polarizabilities

We use the following notations for medium parameters and their relations to permittivity and permeability: ε_p is the nanoparticle permittivity; μ_p is the nanoparticle permeability; $k_p = n_p k_0$ is the effective propagation constant inside the nanoparticle with index n_p of the free-space wave with propagation constant k_0; $n_p = \sqrt{\varepsilon_p \mu_p}$ if $\varepsilon_p > 0, \mu_p > 0$, $n_p = n_{\mathrm{NIM}} = -\sqrt{\varepsilon_p \mu_p}$ if $\varepsilon_p < 0, \mu_p < 0$; ε_e is the permittivity of the surrounding medium; μ_e is the permeability of the surrounding medium; $k_s = n_s k_0$ is the effective propagation constant in the medium with an index n_s of the free-space wave with propagation constant k_0; $n_s = \sqrt{\varepsilon_e \mu_e}$ if $\varepsilon_e > 0, \mu_e > 0$; and $n_s = n_{\mathrm{NIM}} = -\sqrt{\varepsilon_e \mu_e}$ if $\varepsilon_e < 0, \mu_e < 0$. The electric a_n and magnetic b_n Mie coefficients of a spherical nanoparticle are defined as

$$a_n = \frac{m^2 j_n(mx)[x j_n(x)]' - (\mu_p/\mu_e) j_n(x)[mx j_n(mx)]'}{m^2 j_n(mx)[x h_n^{(1)}(x)]' - (\mu_p/\mu_e) h_n^{(1)}(x)[mx j_n(mx)]'},$$

$$b_n = \frac{(\mu_p/\mu_e) j_n(mx)[x j_n(x)]' - j_n(x)[mx j_n(mx)]'}{(\mu_p/\mu_e) j_n(mx)[x h_n^{(1)}(x)]' - h_n^{(1)}(x)[mx j_n(mx)]'}.$$

Here, the functions $j_n(z)$ and $h_n^{(1)}(z) = j_n(z) + i y_n(z)$ are spherical Bessel functions of order n ($n = 1, 2, \ldots$) and given as argument $z = x$ or mx, respectively. The prime sign means derivative with respect to the argument. The parameters are as follows: $m = k_p/k_s$ is the refractive index of the sphere relative to the ambient medium; $x = Rk_s$ is the size parameter; and R is the radius of the sphere. A nonmagnetic case of nanoparticles in the lattice has been derived elsewhere. Here, we show generalized expressions for the case where nanoparticles are surrounded by media with k_s. The polarizabilities of ED, MD, EQ, and MQ of a single nanoparticle are denoted as a_p, a_m, a_Q, and a_M, correspondingly, and they are defined through electric and magnetic Mie coefficients as

$$a_p = i\frac{6\pi\varepsilon_0}{k_0^2 k_s^3} a_1, \quad a_m = i\frac{6\pi}{k_s^3} b_1, \quad a_Q = i\frac{120\pi\varepsilon_0}{k_0^2 k_s^5} a_2, \text{ and } \quad a_M = i\frac{40\pi}{k_s^5} b_2.$$

2. Analytical expressions for particle array

In the following, we give expressions for the case where the incident wave is polarized along the x direction and normal to the array plane. One can show that lattice sums are

$$S_{pp} = \frac{k_0^2}{4\pi}\sum_{l\neq 0}\frac{e^{ik_s r_l}}{r_l}\left(1 + \frac{i}{k_s r_l} - \frac{1}{k_s^2 r_l^2} - \frac{x_l^2}{r_l^2}\left(-\frac{i3}{k_s r_l} + \frac{3}{k_s^2 r_l^2}\right)\right), \quad S_{mm} = \frac{k_s^2}{4\pi}\sum_{l\neq 0}\frac{e^{ik_s r_l}}{r_l}\left(1 + \frac{i}{k_s r_l} - \frac{1}{k_s^2 r_l^2} - \frac{y_l^2}{r_l^2}\left(-\frac{i3}{k_s r_l} + \frac{3}{k_s^2 r_l^2}\right)\right),$$

$$S_{QQ} = \frac{ik_s k_0^2}{24\pi}\sum_{l\neq 0}\frac{e^{ik_s r_l}}{r_l^2}\left(-2 - i\frac{6 + k_s^2 x_l^2}{k_s r_l} + \frac{12 + 7k_s^2 x_l^2}{k_s^2 r_l^2} + i\frac{12 + 27k_s^2 x_l^2}{k_s^3 r_l^3} - \frac{60x_l^2}{k_s^2 r_l^4} - \frac{i60x_l^2}{k_s^3 r_l^5}\right),$$

$$S_{MM} = \frac{ik_s^3}{8\pi}\sum_{l\neq 0}\frac{e^{ik_s r_l}}{r_l^2}\left(-2 - i\frac{6 + k_s^2 y_l^2}{k_s r_l} + \frac{12 + 7k_s^2 y_l^2}{k_s^2 r_l^2} + i\frac{12 + 27k_s^2 y_l^2}{k_s^3 r_l^3} - \frac{60y_l^2}{k_s^2 r_l^4} - \frac{i60y_l^2}{k_s^3 r_l^5}\right),$$

$$S_{mQ} = \frac{k_s^2}{24\pi}\sum_{l\neq 0}\frac{x_l^2 e^{ik_s r_l}}{r_l^3}\left(-1 - \frac{3i}{k_s r_l} + \frac{3}{k_s^2 r_l^2}\right), \quad S_{Qm} = 6S_{mQ},$$

$$S_{pM} = \frac{-k_s^2}{8\pi}\sum_{l\neq 0}\frac{y_l^2 e^{ik_s r_l}}{r_l^3}\left(-1 - \frac{3i}{k_s r_l} + \frac{3}{k_s^2 r_l^2}\right), \text{ and } \quad S_{Mp} = 2S_{pM}.$$

The effective polarizabilities of particles in the lattice without taking into account cross-multipolar coupling can be expressed as

$$\frac{1}{\alpha_p^{\mathrm{eff}}} = \frac{1}{\alpha_p} - \frac{S_{pp}}{\varepsilon_0}, \quad \frac{1}{\alpha_m^{\mathrm{eff}}} = \frac{1}{\alpha_m} - S_{mm}, \quad \frac{1}{\alpha_Q^{\mathrm{eff}}} = \frac{1}{\alpha_Q} - \frac{S_{QQ}}{2\varepsilon_0}, \quad \text{and} \quad \frac{1}{\alpha_M^{\mathrm{eff}}} = \frac{1}{\alpha_M} - \frac{S_{MM}}{2}.$$

In turn, the effective polarizabilities of particles in the lattice that account for cross-multipolar coupling are defined as

$$\frac{1}{\alpha_p^{\mathrm{eff/coup}}} = \frac{1}{\alpha_p^{\mathrm{eff}}}\frac{1 - S_{Mp}\alpha_p^{\mathrm{eff}} S_{pM}\alpha_M^{\mathrm{eff}} k_0^2/(2\varepsilon_0)}{1 - S_{pM}\alpha_M^{\mathrm{eff}} k_s^2/2}, \quad \frac{1}{\alpha_m^{\mathrm{eff/coup}}} = \frac{1}{\alpha_m^{\mathrm{eff}}}\frac{1 - S_{Qm}\alpha_m^{\mathrm{eff}} S_{mQ}\alpha_Q^{\mathrm{eff}} k_0^2/(2\varepsilon_0)}{1 + S_{mQ}\alpha_Q^{\mathrm{eff}} k_0^2/(2\varepsilon_0)},$$

$$\frac{1}{\alpha_Q^{\mathrm{eff/coup}}} = \frac{1}{\alpha_Q^{\mathrm{eff}}} \frac{1 - S_{Qm}\alpha_m^{\mathrm{eff}} S_{mQ}\alpha_Q^{\mathrm{eff}} k_0^2/(2\varepsilon_0)}{1 + S_{Qm}\alpha_m^{\mathrm{eff}}}, \text{ and } \frac{1}{\alpha_M^{\mathrm{eff/coup}}} = \frac{1}{\alpha_M^{\mathrm{eff}}} \frac{1 - S_{Mp}\alpha_p^{\mathrm{eff}} S_{pM}\alpha_M^{\mathrm{eff}} k_0^2/(2\varepsilon_0)}{1 - S_{Mp}\alpha_p^{\mathrm{eff}} k_0^2/(k_s^2\varepsilon_0)}.$$

Finally, considering the array with the periods D_x and D_y, the reflectance and transmittance coefficients are defined as

$$r_0 = \frac{ik_s}{2D_xD_y}\left[\frac{k_{0z}^2}{\varepsilon_0 k_s^2}\alpha_p^{\mathrm{eff/coup}} - \alpha_m^{\mathrm{eff/coup}} - \frac{k_0^2}{12\varepsilon_0}\alpha_Q^{\mathrm{eff/coup}} + \frac{k_s^2}{4}\alpha_M^{\mathrm{eff/coup}}\right],$$

$$t_0 = 1 + \frac{ik_s}{2D_xD_y}\left[\frac{k_0^2}{\varepsilon_0 k_s^2}\alpha_p^{\mathrm{eff/coup}} + \alpha_m^{\mathrm{eff/coup}} + \frac{k_0^2}{12\varepsilon_0}\alpha_Q^{\mathrm{eff/coup}} + \frac{k_s^2}{4}\alpha_M^{\mathrm{eff/coup}}\right].$$

In our analysis above, we have considered a high-refractive-index nanoparticle surrounded by NIM with varying refractive indices and have shown that this structure and optical phenomena can be realized in real life with metamaterials that effectively mimic NIM. From the point of view of physics, one can inquire about the optical properties and multipolar resonances of the NIM spheres in different surrounding media. To address this question, we consider two other systems complementary to those considered above. The calculations in Fig. 5(a) show that the NIM sphere with $\varepsilon_p = -12$ and $\mu_p = -1$ in the NIM surrounding space with $\varepsilon_e = -1$ and $\mu_e = -1$ has the same reflectance and transmittance spectra as a silicon sphere in air ($\varepsilon_p = 12$, $\mu_p = 1$, $\varepsilon_e = \mu_e = 1$). Similarly, the NIM sphere with $\varepsilon_p = -12$ and $\mu_p = -1$ in air ($\varepsilon_e = \mu_e = 1$) has the same spectra as a silicon sphere ($\varepsilon_p = 12$ and $\mu_p = 1$) in NIM surrounding with $\varepsilon_e = -1$ and $\mu_e = -1$ [Fig. 5(b)]. If the signs of permittivity and permeability of the nanoparticle and surrounding medium are reversed simultaneously, the reflectance and transmittance spectra of the nanoparticle array do not change. This observation reflects the invariance of Maxwell's equations with respect to the simultaneous change in the sign of the permittivity and permeability of the nanoparticle medium and the array host surrounding.

REFERENCES

[1] I. Staude, A. E. Miroshnichenko, M. Decker, N. T. Fofang, S. Liu, E. Gonzales, J. Dominguez, T. S. Luk, D. N. Neshev, I. Brener, and Y. Kivshar, "Tailoring directional scattering through magnetic and electric resonances in subwavelength silicon nanodisks," ACS Nano **7**, 7824 (2013).

[2] P. Offermans, M. C. Schaafsma, S. R. K. Rodriguez, Y. Zhang, M. Crego-Calama, S. H. Brongersma, and J. Gómez-Rivas, "Universal scaling of the figure of merit of plasmonic sensors," ACS Nano **5**, 5151 (2011).

[3] D. Bosomtwi, M. Osin´ski, and V. E. Babicheva, "Lattice effect for enhanced hot-electron generation in nanoelectrodes," Opt. Mater. Express **11**(9), 3232–3244 (2021).

[4] A. V. Chebykin *et al.*, "Enhancement of the Purcell factor in multiperiodic hyperboliclike metamaterials," Phys. Rev. A **93**, 033855 (2016).

[5] S. V. Zhukovsky *et al.*, "Giant photogalvanic effect in noncentrosymmetric plasmonic nanoparticles," Phys. Rev. X **4**(3), 031038 (2014).

[6] A. Han, C. Dineen *et al.*, "Second harmonic generation in metasurfaces with multipole resonant coupling," Nanophotonics **9**(11), 3545–3556 (2020).

[7] M. J. Kyamo, A. A. Alsalhin, N. Premkumar, S. Miao, and B. A. Lail, "Ultrahigh mid-infrared electric field enhancement via nanoantenna plasmonic resonance coupled to a novel hyperbolic metalens," J. Mod. Opt. **68**(7), 394–402 (2021).

[8] Q. Jin, G. Liang, W. Kong, L. Liu, Z. Wen, Y. Zhou, C. Wang, G. Chen, and X. Luo, "Negative index metamaterial at ultraviolet range for subwavelength photolithography," Nanophotonics **11**(8), 1643–1651 (2022).

[9] A. B. Evlyukhin, S. M. Novikov, U. Zywietz, R. L. Eriksen, C. Reinhardt, S. I. Bozhevolnyi, and B. N. Chichkov, "Demonstration of magnetic dipole resonances of dielectric nanospheres in the visible region," Nano Lett. **12**, 3749 (2012).

[10] A. B. Evlyukhin, C. Reinhardt, A. Seidel, B. S. Luk'yanchuk, and B. N. Chichkov, "Optical response features of Si-nanoparticle arrays," Phys. Rev. B **82**, 045404 (2010).

[11] A. Baev, P. N. Prasad, H. Ågren, M. Samoc´, and M. Wegener, "Metaphotonics: An emerging field with opportunities and challenges," Phys. Rep. **594**, 1–60 (2015).

[12] D. G. Baranov, R. S. Savelev, S. V. Li, A. E. Krasnok, and A. Alù, "Modifying magnetic dipole spontaneous emission with nanophotonic structures," Laser Photonics Rev. **11**, 1600268 (2017).

[13] M. Kerker, D. S. Wang, and C. L. Giles, "Electromagnetic scattering by magnetic spheres," J. Opt. Soc. Am. **73**, 765 (1983).

[14] G. V. Eleftheriades, M. Kim, V. G. Ataloglou, and A. H. Dorrah, "Prospects of huygens' metasurfaces for antenna applications," Engineering **11**, 21–26 (2022).

[15] V. E. Babicheva and J. V. Moloney, "Lattice Zenneck modes on subwavelength antennas," Laser Photonics Rev. **13**(2), 1800267 (2019).

[16] J. B. Pendry, "Negative refraction makes a perfect lens," Phys. Rev. Lett. **85**, 3966 (2000).

[17] V. M. Shalaev, "Optical negative-index metamaterials," Nat. Photonics **1**, 41–48 (2007).

[18] J. B. Pendry, "Negative refraction," Contemp. Phys. **45**, 191 (2004).

[19] S. Liu, Z. Ma, J. Pei, Q. Jiao, L. Yang, W. Zhang, H. Li, Y. Li, Y. Zou, and X. Tan, "A review of anomalous refractive and reflective metasurfaces," Nanotechnol. Precis. Eng. **5**(2), 025001 (2022).

[20] H. J. Lezec, J. A. Dionne, and H. A. Atwater, "Negative refraction at visible frequencies," Science **316**, 430–432 (2007).

[21] H. Pashaei Adl, S. Gorji, A. F. Gualdrón-Reyes, I. Mora-Seró, I. Suárez, and J. P. Martínez-Pastor, "Enhanced spontaneous emission of $CsPbI_3$ perovskite nanocrystals using a hyperbolic metamaterial modified by dielectric nanoantenna," Nanomaterials **13**, 11 (2023).

[22] J. A. Dionne, E. Verhagen, A. Polman, and H. A. Atwater, "Are negative index materials achievable with surface plasmon waveguides? A case study of three plasmonic geometries," Opt. Express **16**, 19001–19017 (2008).

[23] H. Shin and S. Fan, "All-angle negative refraction for surface plasmon waves using a metal-dielectric-metal structure," Phys. Rev. Lett. **96**, 073907 (2006).

[24] V. E. Babicheva, "Long-range propagation of plasmon and phonon polaritons in hyperbolic-metamaterial waveguides," J. Opt. **19**, 124013 (2017).

[25] A. A. Orlov, A. K. Krylova, S. V. Zhukovsky *et al.*, "Multiperiodicity in plasmonic multilayers: General description and diversity of topologies," Phys. Rev. A **90**, 013812 (2014).

[26] J. Valentine, S. Zhang, T. Zentgraf, E. Ulin-Avila, D. A. Genov, G. Bartal, and X. Zhang, "Three-dimensional optical metamaterial with a negative refractive index," Nature **455**, 376 (2008).

[27] C. Helgert, C. Menzel, C. Rockstuhl, E. Pshenay-Severin, E.-B. Kley, A. Chipouline, A. Tünnermann, F. Lederer, and T. Pertsch, "Polarization-independent negative-index metamaterial in the near infrared," Opt. Lett. **34**, 704–706 (2009).

[28] W. J. Padilla, D. N. Basov, and D. R. Smith, "Negative refractive index metamaterials," Mater. Today **9**, 28–35 (2006).

[29] A. Alù, A. Salandrino, and N. Engheta, "Negative effective permeability and left-handed materials at optical frequencies," Opt. Express **14**, 1557–1567 (2006).

[30] V. M. Shalaev, W. Cai, U. K. Chettiar, H.-K. Yuan, A. K. Sarychev, V. P. Drachev, and A. V. Kildishev, "Negative index of refraction in optical metamaterials," Opt. Lett. **30**, 3356–3358 (2005).
[31] Y. Liu, G. P. Wang, J. B. Pendry, and S. Zhang, "All-angle reflectionless negative refraction with ideal photonic Weyl metamaterials," Light Sci. Appl. **11**, 276 (2022).
[32] S. P. Burgos, R. deWaele, A. Polman, and H. A. Atwater, "A single-layer wide-angle negative-index metamaterial at visible frequencies," Nat. Mater. **9**, 407 (2010).
[33] A. Bhardwaj, N. M. Puthoor, and G. G. Nair, "Tunable directional scattering from high-refractive-index particles dispersed in an anisotropic medium," J. Phys. Chem. C **124**, 18698–18706 (2020).
[34] V. Bruno, C. DeVault, S. Vezzoli, Z. Kudyshev, T. Huq, S. Mignuzzi, A. Jacassi, S. Saha, Y. D. Shah, S. A. Maier, D. R. S. Cumming, A. Boltasseva, M. Ferrera, M. Clerici, D. Faccio, R. Sapienza, and V. M. Shalaev, "Negative refraction in time-varying strongly coupled plasmonic-antenna–epsilon-near-zero systems," Phys. Rev. Lett. **124**, 043902 (2020).
[35] Y. Ma, G. Zhong, Z. Dai, and Q. Ou, "In-plane hyperbolic phonon polaritons: Materials, properties, and nanophotonic devices," npj Nanophotonics **1**, 25 (2024).
[36] Y. Wu, J. Liu, W. Yu, T. Zhang, H. Mu, G. Si, Z. Cui, S. Lin, B. Zheng, C.-W. Qiu, H. Chen, and Q. Ou, "Monolithically structured van der Waals materials for volume-polariton refraction and focusing," ACS Nano **18**(26), 17065–17074 (2024).
[37] T. Zhang, C. Zheng, Z. N. Chen, and C.-W. Qiu, "Negative reflection and negative refraction in biaxial van der Waals materials," Nano Lett. **22**, 5607–5614 (2022).
[38] R.-T. Liu and C.-C. Huang, "Interfacing differently oriented biaxial van der Waals crystals for negative refraction," Nanophotonics **12**(21), 4063–4072 (2023).
[39] A. J. Sternbach, S. L. Moore, A. Rikhter *et al.*, "Negative refraction in hyperbolic hetero-bicrystals," Science **379**, 555–557 (2023).
[40] H. Rubinsztein-Dunlop *et al.*, "Roadmap on structured light," J. Opt. **19**, 013001 (2017).
[41] N. M. Litchinitser, "Structured light meets structured matter," Science **337**, 1054–1055 (2012).
[42] A. B. Evlyukhin, C. Reinhardt, U. Zywietz, and B. N. Chichkov, "Collective resonances in metal nanoparticle arrays with dipole-quadrupole interactions," Phys. Rev. B **85**, 245411 (2012).
[43] I. Allayarov, A. B. Evlyukhin, and A. Calà Lesina, "Multiresonant all-dielectric metasurfaces based on high-order multipole coupling in the visible," Opt. Express **32**(4), 5641–5658 (2024).
[44] A. Han, J. V. Moloney, and V. E. Babicheva, "Applicability of multipole decomposition to plasmonic- and dielectric-lattice resonances," J. Chem. Phys. **156**, 114104 (2022).
[45] C. F. Bohren and D. R. Huffman, *Absorption and Scattering of Light by Small Particles* (John Wiley & Sons, 2008).
[46] D. C. Tzarouchis, P. Ylä-Oijala, and A. Sihvola, "Resonant scattering characteristics of homogeneous dielectric sphere," IEEE Trans. Antennas Propag. **65**, 3184–3191 (2017).
[47] C. A. Valagiannopoulos, "Single-series solution to the radiation of loop antenna in the presence of a conducting sphere," Prog. Electromagn. Res. **71**, 277–294 (2007).
[48] G. C. Kokkorakis and J. G. Fikioris, "EM field induced in inhomogeneous dielectric spheres by external sources," IEEE Trans. Antennas Propag. **55**(11), 3178–3190 (2007).
[49] N. L. Tsitsas and C. A. Valagiannopoulos, "Anomalous reflection of visible light by all-dielectric gradient metasurfaces," J. Opt. Soc. Am. B **34**, D1–D8 (2017).
[50] Y. K. Chiang, S. Oberst, A. Melnikov, L. Quan, S. Marburg, A. Alù, and D. A. Powell, "Reconfigurable acoustic metagrating for high-efficiency anomalous reflection," Phys. Rev. Appl. **13**, 064067 (2020).
[51] Y. Li and C. Argyropoulos, "Tunable nonlinear coherent perfect absorption with epsilon-near-zero plasmonic waveguides," Opt. Lett. **43**, 1806–1809 (2018).
[52] I. Katsantonis, A. C. Tasolamprou, T. Koschny, E. N. Economou, M. Kafesaki, and C. Valagiannopoulos, "Giant enhancement of nonreciprocity in gyrotropic heterostructures," Sci. Rep. **13**, 21986 (2023).